©2022 Society of Economic Geologists, Inc.
Economic Geology, v. 117, no. 2, pp. 495–508

FEASIBILITY OF VISIBLE SHORT-WAVE INFRARED REFLECTANCE SPECTROSCOPY TO CHARACTERIZE REGOLITH-HOSTED RARE EARTH ELEMENT MINERALIZATION

Wei Tan,[1] Xiaorong Qin,[1,2] Jiacheng Liu,[3,4] Mei-Fu Zhou,[3] Hongping He,[1,†] Christina Yan Wang,[1] Jian Huang,[1,2] Jianxi Zhu,[1,2] Yuzeng Yao,[5] and Thomas Cudahy[6]

[1]*Key Laboratory of Mineralogy and Metallogeny/Guangdong Provincial Key Laboratory of Mineral Physics and Materials, Guangzhou Institute of Geochemistry, Chinese Academy of Sciences, Guangzhou 510640, China*

[2]*University of Chinese Academy of Sciences, Beijing 100049, China*

[3]*Department of Earth Sciences, The University of Hong Kong, Pokfulam Road, Hong Kong*

[4]*Division of Earth and Planetary Science and Laboratory for Space Research, The University of Hong Kong, Hong Kong*

[5]*School of Resources and Civil Engineering, Northeastern University, Shenyang 110819, China*

[6]*C3DMM Pty Ltd., 3/473 Cambridge Street Floreat, Western Australia 6014, Australia*

Abstract

Regolith-hosted rare earth element (REE) deposits predominate global resources of heavy REEs. Regoliths are underlain by various types of igneous rocks and do not always host economically valuable deposits. Thus a feasible and convenient method is desired to identify REE mineralization in a particular regolith. This study presents a detailed visible short-wave infrared reflectance (VSWIR) spectroscopic study of the Renju regolith-hosted REE deposit, South China, to provide diagnostic parameters for targeting REE orebodies in regoliths. The results show that the spectral parameters, M794_2nd and M800_2nd, derived from the VSWIR absorption of Nd^{3+} at approximately 800 nm, can be effectively used to estimate the total REE concentrations in regolith profiles. M1396_2nd/M1910_2nd ratios can serve as proxies to evaluate weathering intensities in a regolith. Abrupt changes of specific spectral features related to mineral abundances, chemical compositions, and weathering intensities can be correlated with variations of protolith that formed a regolith. These VSWIR proxies are robust and can be used for exploration of regolith-hosted REE deposits.

Introduction

Regolith-hosted rare earth element (REE) deposits account for approximately 20% of China's REE production and represent a major global source of heavy REEs (Sanematsu and Watanabe, 2016; Xie et al., 2016; Xu et al., 2017). These deposits were thought to have formed by weathering of biotite/muscovite granite, syenite, monzogranite, granodiorite, granite porphyry, and rhyolitic tuff (Bao and Zhao, 2008; Li et al., 2017). REEs released from REE-bearing minerals in protolith are leached downward via continuous infiltration of meteoric water and are eventually adsorbed by supergene minerals to form economical orebodies in semiweathered and/or completely weathered zones (Li et al., 2017). Thus, weathering intensities and protolith variations are also important factors controlling the distributions of REE orebodies in regoliths. Exploration for regolith-hosted REE deposits requires extensive analyses of REE concentrations and information on weathering intensities and protolith variations of regoliths to locate orebodies.

Routine exploration strategies utilizing REE concentrations, weathering intensities, and protolith variations of a regolith are time-consuming and expensive to obtain, as laboratory-based analyses (e.g., X-ray diffraction, X-ray fluorescence spectrometry, and inductively coupled plasma-mass spectrometry) are extensively required. Visible and short-wave infrared reflectance (VSWIR) spectroscopy is a rapid and economical technique that has been widely used as an exploration tool to identify deposit-scale hydrothermal alteration and mineralization zones, particularly of porphyry copper deposits (Herrmann et al., 2001; Jones et al., 2005; Jansen et al., 2017). This technique may be applicable to exploration of regolith-hosted REE deposits but has not been fully evaluated.

The VSWIR spectrum includes the short-wave infrared region (1,000–2,500 nm) and visible and near-infrared region (350–1,000 nm) (Cudahy, 2016). The short-wave infrared region includes diagnostic features of clay minerals (Hunt, 1977; Hunt and Ashley, 1979; Clark et al., 1990; Liu et al., 2021), and the visible and near-infrared region includes absorption bands of transition element-bearing oxides/oxyhydroxides (e.g., hematite and goethite) (Cudahy and Ramanaidou, 1997) and REE-bearing minerals (Turner et al., 2014, 2016, 2018; Neave et al., 2016; Möller and Williams-Jones, 2018). These minerals occur widely in regolith-hosted REE deposits, and thus it is possible that the VSWIR spectrum can be used to prospect for such deposits, especially if the equipment is mounted on hyperspectral remote sensing platforms (Cudahy, 2016; Neave et al., 2016, Möller and Williams-Jones, 2018). However, due to the lack of knowledge of the fundamental VSWIR parameters to characterize REE concentrations, weathering intensities, and protolith variations of regoliths, the feasibility of the VSWIR spectrum for prospecting regolith-hosted REE deposits has yet to be tested.

In this paper, we use the VSWIR spectroscopy to examine a regolith profile from the Renju regolith-hosted REE deposit in South China. Samples are taken from a 78-m-long drill hole that penetrated a complete regolith profile from the bedrock to top soils. Our study demonstrates that the VSWIR spectroscopy can be feasibly applied for exploration of regolith-hosted REE deposits and provide effective VSWIR parameters to accurately characterize a regolith profile,

†Corresponding author: e-mail, hehp@gig.ac.cn

 Submitted: December 14, 2020 / Accepted: June 1, 2021

Downloaded from http://pubs.geoscienceworld.org/segweb/economicgeology/article-pdf/117/2/495/5505776/4877_tan_et_al.pdf
by Guangzhou Institute of Geochemistry CAS user

including REE concentrations, weathering intensities, and protolith variations.

Renju Regolith-Hosted REE Deposit

The Renju deposit is located in northeast Guangdong province, neighboring the Jiangxi and Fujian provinces in South China (Fig. 1). The South China block consists of the Yangtze block in the northwest and the Cathaysia block in the southeast, with a Precambrian basement covered by Cambrian to Cenozoic supracrustal sequences. South China has experienced multiple episodes of tectonothermal events and is characterized by vast amounts of Mesozoic granitic plutons and associated volcanic rocks (Li et al., 2017).

In the Renju region, a Precambrian basement is covered by Cambrian to Cretaceous sedimentary successions and Quaternary deposits (Fig. 1). These sedimentary sequences are intruded by early Paleozoic granitic plutons and Mesozoic plutons composed of granite porphyry and medium- and fine-grained biotite granite (Fig. 1). Mesozoic rhyolitic tuff is also widely exposed in the region (Fig. 1).

The Renju region has an East Asian monsoon subtropical climate with a mean annual temperature of 25°C and a mean annual precipitation of 1,500–2,000 mm, which facilitates enrichment of ion adsorption-type REEs in regoliths via intense chemical weathering of protolith (Sanematsu and Watanabe, 2016). Weathering of biotite granite, granite porphyry, and rhyolitic tuff contributes to the ore formation.

The Renju deposit is a typical regolith-hosted REE deposit in South China. This deposit contains total ore reserves of 80,000 t with an average ore grade of total REEs ranging from 800 to 1,300 ppm (Meng et al., 2016). About 75% of the total REEs are ion adsorption-type REEs hosted by clay minerals (Yang and Xiao, 2011). Orebodies are distributed as crescent-shaped lenses with an average thickness of 5–6 m in the regoliths.

The investigated regolith profile at Renju includes, from the base upward, weathered bedrock (78–62 m depth), a semiweathered zone (62–10 m depth), a completely weathered zone (10–1 m depth), and a lateritic zone (above 1 m depth) (Fig. 2). The semiweathered zone can be further divided into three subzones (SZ-I, SZ-II, and SZ-III) based on variations of supergene minerals (Fig. 2). In this study, 53 samples were collected from a 78-m-long drill hole that penetrated a complete regolith profile, 24 samples were collected at intervals of 0.5–1.0 m at depths of 0–20 m, and 29 samples were collected at intervals of 2.0 m at depths of 20–78 m.

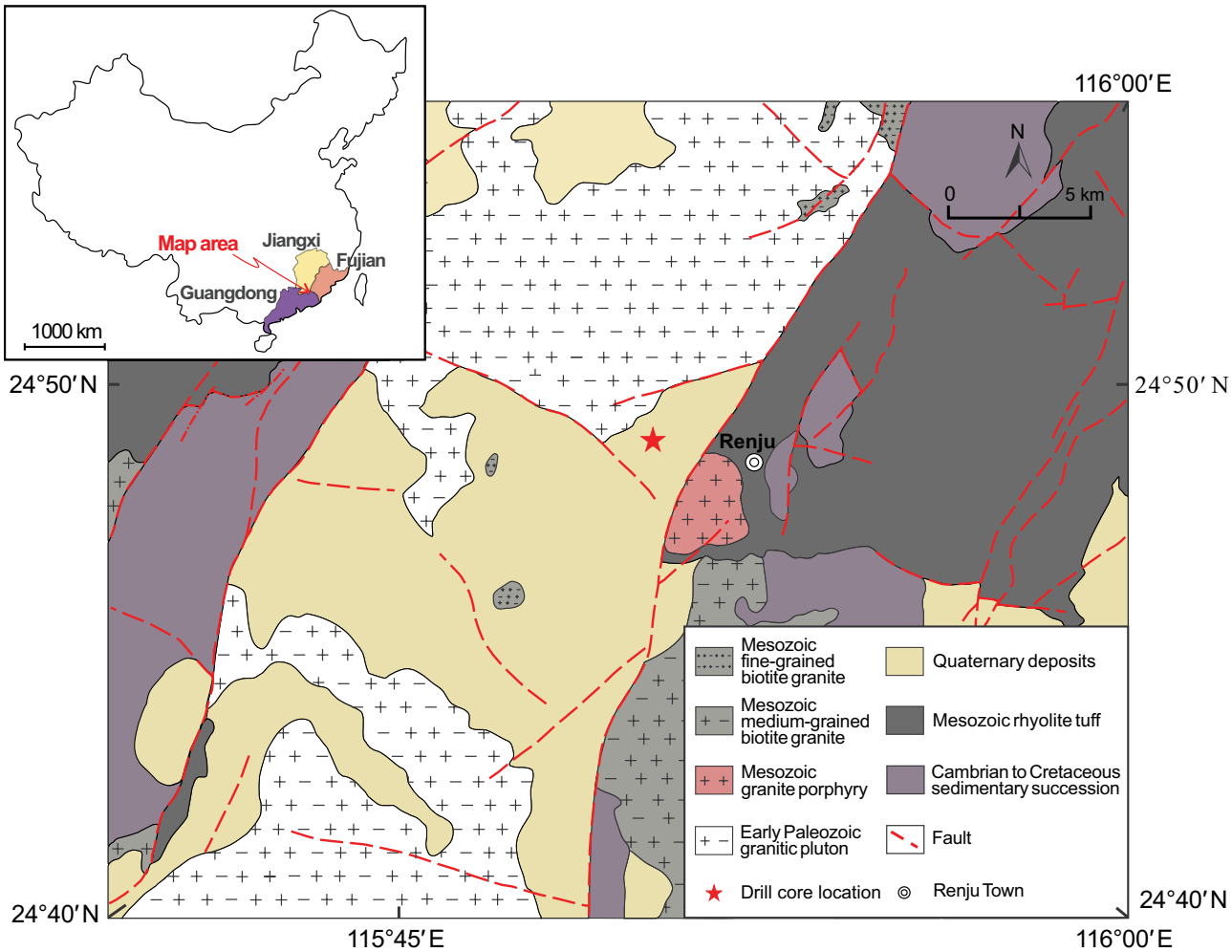

Fig. 1. Simplified geologic map of the Renju rare earth element deposit (after Regional Geological Survey Team of Jiangxi Geological Bureau, 1976). Sample location is N24°48'7" and E115°50'8".

Downloaded from http://pubs.geoscienceworld.org/segweb/economicgeology/article-pdf/117/2/495/5505776/4877_tan_et_al.pdf
by Guangzhou Institute of Geochemistry CAS user

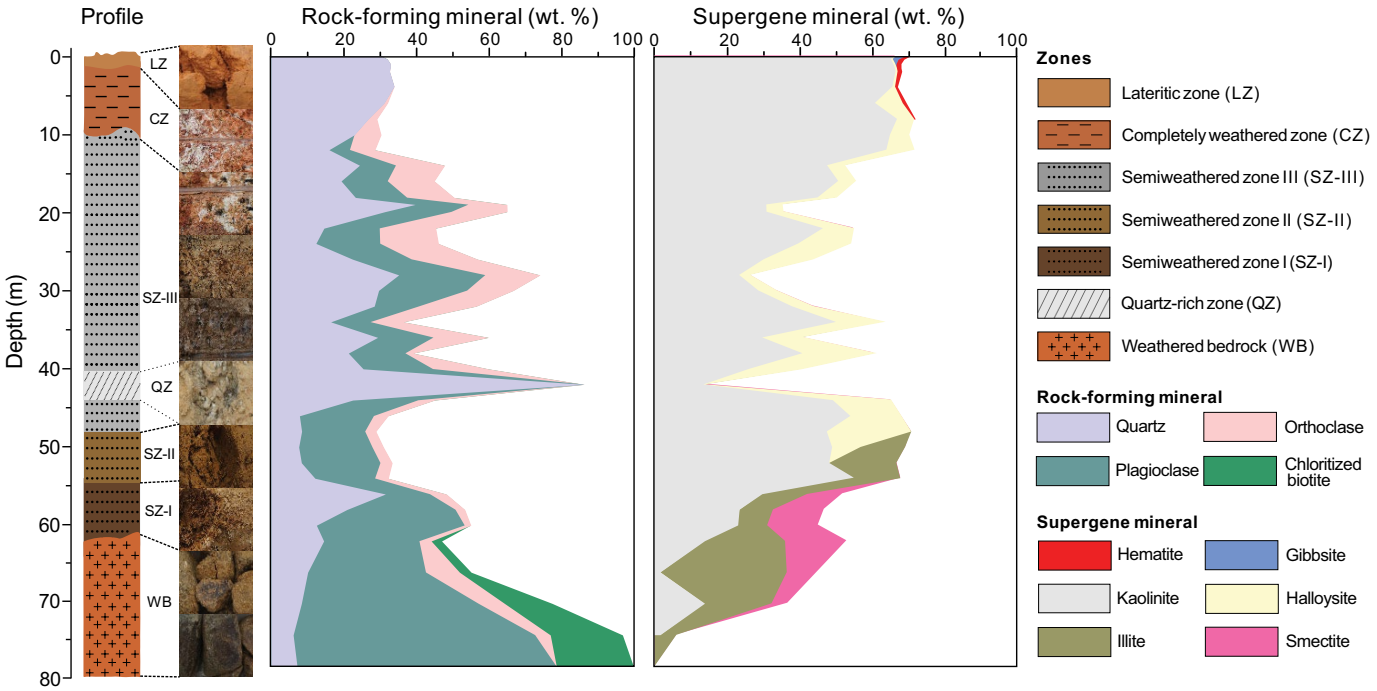

Fig. 2. Stratigraphic column of the profile of the Renju rare earth element deposit showing distributions of rock-forming and supergene minerals.

Methods

Mineral abundances

Samples from the drill core were dried at room temperature and manually pulverized with an agate mortar and pestle to approximately 50-μm-grain-size powder. The powdered samples were further selected for estimating mineral abundances and analyses of major and trace element concentrations. X-ray diffraction (XRD) analyses were performed with a Bruker D8 Advance X-ray diffractometer with Cu/Kα radiation and an Ni filter operating at a current of 40 mA and voltage of 40 kV. The XRD patterns were recorded between 3° and 80° (2θ) at a scanning speed of 3°/min. JADE 6.5 software was used to determine the peak intensity specified for each mineral phase. Semiquantitative analyses were performed using the peak intensity of each crystalline phase with the reference intensity ratio methods (cf. Tamer, 2013).

Whole-rock major element concentrations and weathering intensities

Powdered samples were heated at 900°C for 90 min to remove organic matter and carbonate. Approximately 0.50 g of each pretreated sample was then weighed, mixed with 4.00 g $Li_2B_4O_7$, and fused into glass disks at 1,200°C. Major elements were measured from the glass disks with a Rigaku ZSX100e X-ray fluorescence spectrometer. The analytical procedures were similar to those described in Ramsey et al. (1995). The analytical precisions for major elements are better than 1%.

Weathering intensities are evaluated by the chemical index of alteration (CIA = $Al_2O_3/[Al_2O_3 + K_2O + Na_2O + CaO] \times 100$; cf. Nesbitt and Young, 1982), using the whole-rock major element concentrations of the samples collected at different depths in the regolith profile.

Whole-rock REE concentrations

Powdered samples were dried at 105°C for 3 h and baked at 550°C for 3 h to eliminate organic materials. Approximately 0.04 g of each solid sample was placed into a precleaned 15-ml Teflon beaker with 1.25 ml HNO_3 + 0.5 ml HF + 0.25 ml $HClO_4$ mixture. The beakers were tightly capped and ultrasonically shaken for 30 min, then the beakers were opened and placed on a hot plate overnight at 100°C. Then 2 ml of HNO_3 + HF +$HClO_4$ mixture was added to the beakers, which were tightly capped again. The beakers were wrapped in a stainless-steel bomb and placed in a baking oven at 190°C for two days to ensure that samples were fully digested. After being dried, samples were fully redissolved with 2 ml 1:1 HNO_3, then diluted with 2% HNO_3 for trace element measurements. Trace elements were analyzed with a Thermo-iCAP quadrupole inductively coupled plasma-mass spectrometer (ICP-MS). Rhodium was added to each sample as an internal standard to monitor the matrix and drift of the machine during measurements. Several U.S. Geological Survey and Chinese rock and sediment standards (GSR-2, GSR-3, GSD-09, GSD-11, SARM-4, W-2, and AGV-2) were used as external standards for quality control. The analytical precisions for trace elements are better than 3%.

VSWIR spectrum

Powdered samples were measured with an Analytical Spectral Devices FieldSpec-3 spectrometer equipped with a circle detector. The spot size was approximately 20 mm. Laboratory measurements were conducted in a dark room under a standard atmosphere, and the reflectance was measured relative to a white plate. Fifty scan acquisitions were set to yield an average spectrum for each measured spectrum to improve

Downloaded from http://pubs.geoscienceworld.org/segweb/economicgeology/article-pdf/117/2/495/5505776/4877_tan_et_al.pdf
by Guangzhou Institute of Geochemistry CAS user

the signal-to-noise ratio. The spectral resolution is 3 nm (full-width-half-maximum) at 700 nm, 10 nm at 1,400 nm, and 10 nm at 2,100 nm. The sampling interval is 1.4 nm for the spectral region 350–1,000 nm, and 2 nm for the spectral region 1,000–2,500 nm. The reference spectra of tested minerals were from the Analytical Spectral Devices spectra library. ViewSpecPro software was used to preprocess the raw spectra, including splice correction and averaging. Note that different instruments may generate 1- to 3-nm differences in the values of VSWIR absorption bands when a spectral parameter is collected from the same mineral (Chang and Yang, 2012). Despite the differences in absolute values, the data sets produced by different instruments tend to show the same variation trends (Chang and Yang, 2012).

The raw spectra are also processed using The Spectral Geologist (TSG) software. The continuum removal approach is used to remove background noise and to isolate specific absorption features for identification and analysis, whereas slight changes in the spectra were overlooked. The Fourier self-deconvolution approach is used to locate the position center (P) and to acquire the band depth (BD; i.e., the distance from baseline to peak) of specific absorption. The second derivative curves of the raw spectra are obtained to highlight slight changes in the original reflectance spectrum (Mathian et al., 2018). The maxima (M) observed in the second derivative curves, which represent inflection points on the VSWIR spectra, are proportional to the intensities of given bands on the raw spectra.

Results

Mineral abundances and bulk sample chemical compositions

The quartz diorite bedrock is transitional to the slightly weathered zone, in which rocks are dark brown (Fig. 2) and have CIA values ranging from 62 to 75 (Fig. 3). In this zone, the slightly weathered quartz diorite (Fig. 4A) is composed of plagioclase (~30–~65 wt %), orthoclase (~1–~5 wt %), quartz (~4–~7 wt %), and chloritized biotite (~2–~20 wt %) (Fig. 2). The weathered bedrocks are usually surrounded by supergene minerals, kaolinite (~2–~15 wt %), illite (<~30 wt %), and smectite (~20 wt %) (Fig. 4B). They have relatively homogeneous chemical compositions, and contain 16–18 wt % Al_2O_3, 55–57 wt % SiO_2, 4–9 wt % Fe_2O_3, and <5 wt % of Na_2O, K_2O, CaO, and MgO (Fig. 3).

In the semiweathered zone, weathered rocks are mottled yellowish red, white, and brown (Fig. 2) and contain approximately 70% clay minerals that progressively increase with progressive weathering intensities (CIA = 75–92) (Fig. 3). The illite-/smectite-bearing SZ-I (Figs. 2, 4C) and illite-bearing SZ-II (Figs. 2, 4D) have significantly low amounts of Na_2O (0–3 wt %), CaO (~0 wt %), and MgO (1–3 wt %) and high amounts of Al_2O_3 (15–23 wt %) and Fe_2O_3 (9–11 wt %) (Fig. 3). The kaolinite-rich SZ-III (Figs. 2, 4E) shows abrupt compositional changes relative to SZ-I and SZ-II, with 12–20 wt % Al_2O_3, 70–80 wt % SiO_2, and 1–2.5 wt % Fe_2O_3 and a decrease of K_2O from ~5.5 to ~1.5 wt % (Fig. 3). A pale, yellow, quartz-rich zone occurs in the SZ-III at depths of 41–44 m and contains >90% SiO_2 (Figs. 2, 4F).

The completely weathered zone has interstratified white and red clay layers (Fig. 4G), with the highest CIA values of 90–100. Hematite appears and gradually increases upward in this zone (Fig. 2). The total abundances of kaolinite and halloysite gradually increase to ~70 wt %, with gradual disappearance of orthoclase (Fig. 2) and a decrease in K_2O from ~1.5 wt % to nearly 0 (Fig. 3). The lateritic zone shows a deep reddish color with an increase in hematite to approximately 1 wt % (Figs. 2, 4H). Gibbsite was found up to approximately

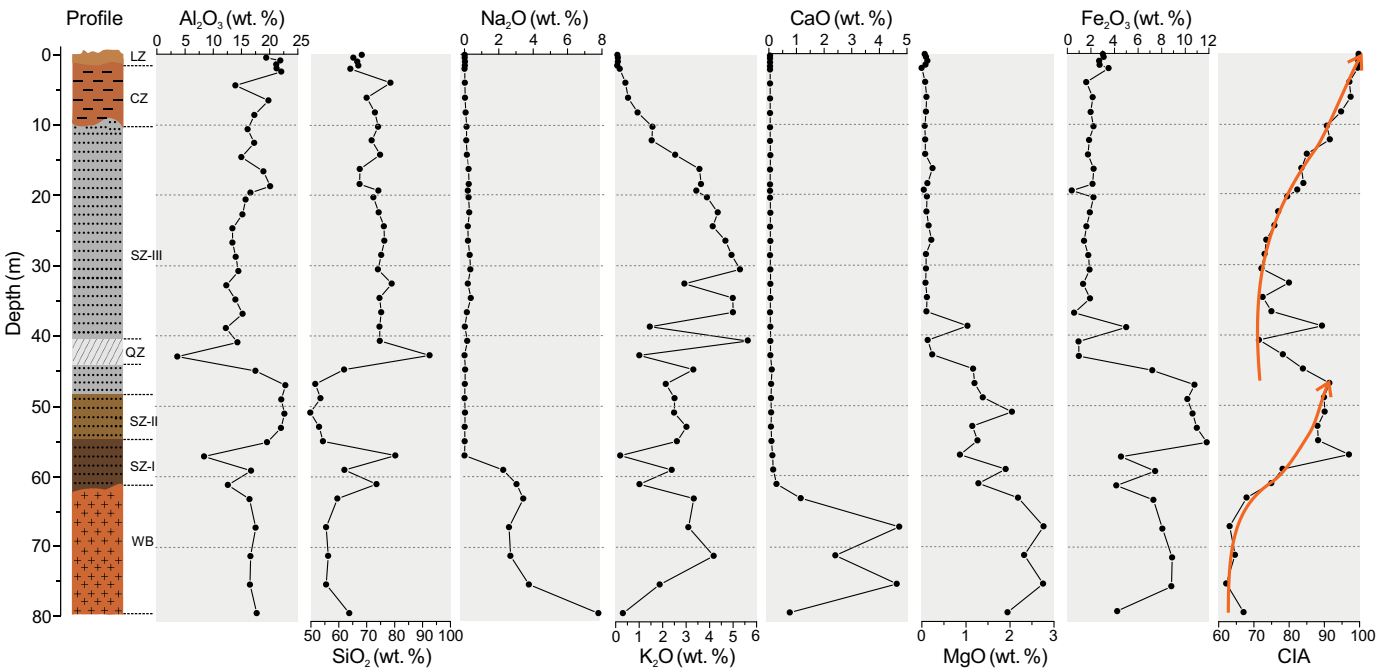

Fig. 3. Variation of Al_2O_3, SiO_2, Na_2O, K_2O, CaO, MgO, and Fe_2O_3, and chemical index of alteration (CIA) values along the profile of the Renju rare earth element deposit. CZ = completely weathered zone, LZ = lateritic zone, QZ = quartz-rich zone, SZ-I/-II/-III = semiweathered zone I/II/III, WB = weathered bedrock.

Downloaded from http://pubs.geoscienceworld.org/segweb/economicgeology/article-pdf/117/2/495/5505776/4877_tan_et_al.pdf
by Guangzhou Institute of Geochemistry CAS user

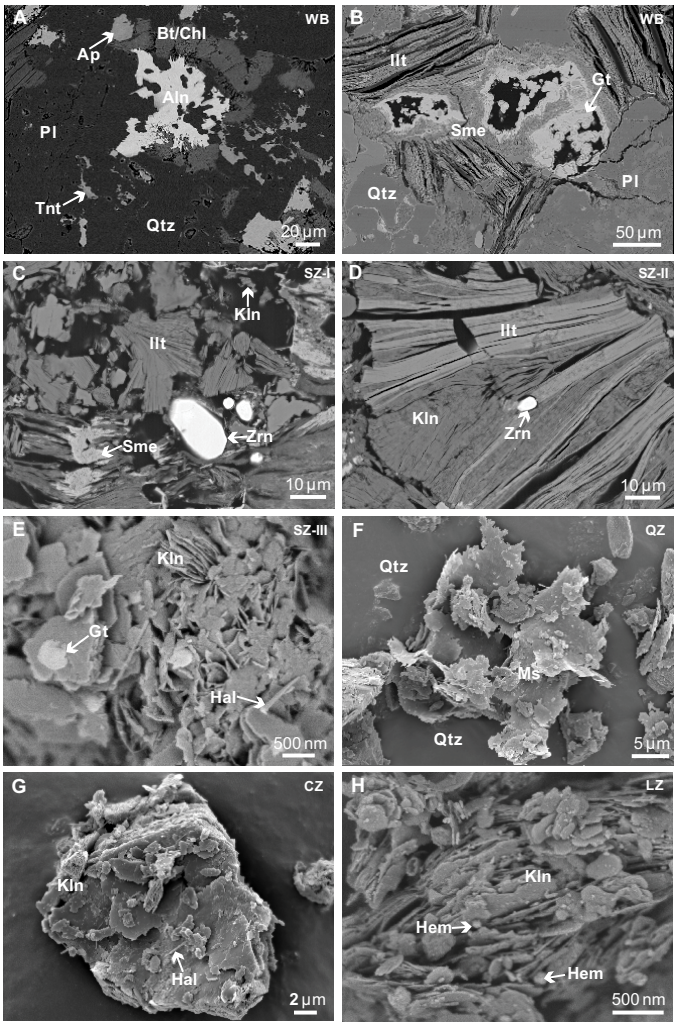

Fig. 4. Scanning electron microscopy images of minerals in the Renju rare earth element (REE) deposit. (A) REE-bearing minerals in weathered bedrock; backscattered electron (BSE) imaging. (B) Supergene minerals (sheeted illite, nanoscale aggregates of smectite and goethite) in weathered bedrock; BSE. (C) Primary zircon and aggregates of supergene minerals (kaolinite and in semiweathered zone I; BSE). (D) Intergrowth of sheeted illite and kaolinite in semiweathered zone II; BSE. (E) Aggregates of sheeted kaolinite, tubular halloysite, and nanoscale goethite in semiweathered zone III; secondary electron (SE) imaging. (F) Occurrences of sheeted muscovite hosted by quartz in the quartz-rich zone; SE. (G) Aggregates of sheeted kaolinite and tubular halloysite in the completely weathered zone; SE. (H) Occurrences of nanoscale hematite particle and sheeted kaolinite in the lateritic zone; SE. Aln = allanite, Ap = apatite, Bt = biotite, Chl = chlorite, CZ = completely weathered zone, Gt = goethite, Hal = halloysite, Hem = hematite, Ilt = illite, Kln = kaolinite, LZ = lateritic zone, Ms = muscovite, Pl = plagioclase, Qtz = quartz, QZ = quartz-rich zone, Sme = smectite, SZ-I/-II/-III = semiweathered zone I/II/III, Tnt = titanite, WB = weathered bedrock, Zrn = zircon.

1 wt % at the top of the lateritic zone (Fig. 2). Correspondingly, the lateritic zone contains more Al_2O_3 (18–22 wt %) and Fe_2O_3 (2–3 wt %) than the completely weathered zone (Fig. 3).

REE concentrations

The weathered bedrock has total REE concentrations from 300 to 450 ppm (Fig. 5A) and displays a typical right-incline chondrite-normalized REE pattern (Fig. 5B). The total REE concentrations range from 100 to 650 ppm in SZ-I and SZ-II, and gradually increase upward in SZ-III from ~500 to ~3,350 ppm (Fig. 5A). SZ-III shows a distinctly negative Ce anomaly relative to the weathered bedrock (Fig. 5C). In contrast, the completely weathered zone and the lateritic zone contain 300 to 600 ppm total REEs (Fig. 5A) with distinctly positive Ce anomalies (Fig. 5D).

VSWIR characteristics of clay minerals

The VSWIR absorptions of clay minerals are derived from overtones and combination tones of the fundamental stretching (ν) and bending (δ) vibrations of hydroxyl (e.g., H_2O, -OH, and Al-OH) (Table 1). All samples exhibit VSWIR absorptions at 1,414 and 2,210 nm (Fig. 6A) contributed by inner-hydroxyl (OH_{inner}) groups and AlAl-OH groups of clay minerals (e.g., kaolinite, illite, and smectite) (Table 1). The weak absorption at around 960 nm (Fig. 6A) corresponds to the second overtone of νOH_{inner} contributed by clay minerals (Clark et al., 1990). The absorption at around 1,910 nm (Fig. 6A) corresponds to the combination tone of molecular water (H-O-H) bending and hydroxyl stretching (νOH) vibrations, which are mostly contributed by clay minerals that contain molecular water (e.g., smectite and illite) (Bishop et al., 2008).

Samples from the weathered bedrock and the lower part of SZ-I show absorptions at around 2,290 nm (Fig. 6B), corresponding to the combination tone of νOH_{inner} and $\delta Fe^{3+}Fe^{3+}$-OH in Fe smectite (Clark et al., 1990). Similarly, the absorption at around 2,240 nm can be attributed to the combination tone of νOH_{inner} and $\delta AlFe^{3+}$-OH of Fe smectite and Fe kaolinite (Delineau et al., 1994; Ramanaidou et al., 2015). Samples collected from the lower part of SZ-I up to the lateritic zone show sharp absorptions at 1,396 and 2,170 nm (Fig. 6A). The absorption at 1,396 nm can be attributed to the first overtone of inner-surface hydroxyl groups' stretching vibration ($\nu OH_{inner\text{-}surface}$) of kaolinite, and the absorption at 2,170 nm can be attributed to the combination tone of $\nu OH_{inner\text{-}surface}$ and δAlAl-OH of kaolinite (Table 1).

Specifically, samples from the quartz-rich zone (Fig. 2) exhibit prominent absorptions at around 2,350 and 2,450 nm (Fig. 6B), which are likely generated by muscovite (Fig. 4F). Samples from the lateritic zone show absorptions at approximately 2,270 nm, likely derived from the Al-OH groups of gibbsite (Clark et al., 1990).

VSWIR characteristics of Fe (hydro)oxide

The VSWIR absorptions at around 500 and 900 nm can be attributed to electron transitions of iron in Fe oxides (e.g., hematite, goethite, and magnetite) and Fe clay minerals (e.g., nontronite and Fe kaolinite) (Cudahy and Ramanaidou, 1997). Generally, hematite and goethite are the dominant Fe-(hydro)oxide phases in the regolith of South China. The XRD analyses demonstrate the presence of hematite in the lateritic zone and the completely weathered zone (Fig. 2), whereas the reflections of goethite could hardly be detected due to its low crystallinity (Schwertmann and Cornell, 2008). The VSWIR absorptions at 520–550 and 860–890 nm are characteristics of hematite, whereas those at 400–480 and 915–960 nm are features of goethite (Hunt and Ashley, 1979; Cudahy and Ramanaidou, 1997). Given that the absorption of clay minerals at around 960 nm (Fig. 6A) can pose an overlapping

Downloaded from http://pubs.geoscienceworld.org/segweb/economicgeology/article-pdf/117/2/495/5505776/4877_tan_et_al.pdf
by Guangzhou Institute of Geochemistry CAS user

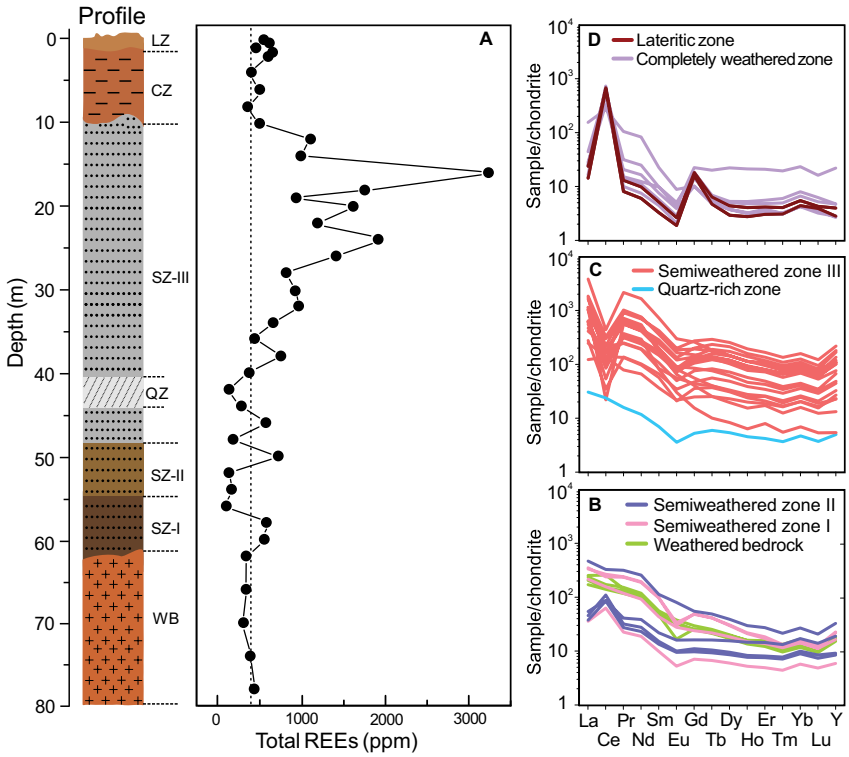

Fig. 5. Rare earth element (REE) concentrations and patterns of different lithological zones along the profile of the Renju REE deposit. (A) Total REE concentrations of rocks. (B) REE patterns of weathered bedrock, semiweathered zone I, and semiweathered zone II. (C) REE patterns of semiweathered zone III and the quartz-rich zone. (D) REE patterns of completely weathered zone and lateritic zone. CZ = completely weathered zone, LZ = lateritic zone, QZ = quartz-rich zone, SZ-I/-II/-III = semiweathered zone I/II/III, WB = weathered bedrock.

problem in determining the band depth and position center of Fe^{3+} absorption at 860–960 nm (Hunt, 1977; Hunt and Ashley, 1979), the Fe^{3+} absorption at approximately 500 nm more effectively identifies and discriminates hematite and goethite. The band depth of absorption at approximately 500 nm (BD500) can be used to determine the abundance of Fe-(hydro)oxides, and the position center (P500) can be used to determine the relative proportions of hematite and goethite (Fig. 6C).

VSWIR characteristics of Nd^{3+}

Samples from the upper part of SZ-III have relatively high REE concentrations (800–3,350 ppm). These samples show absorptions at approximately 740, 800, and 865 nm (Fig. 7A), which correspond to the Nd^{3+} absorptions at approximately 740, 800, and 870 nm in fluorapatite, monazite, and britholite, respectively (Neave et al., 2016; Turner et al., 2018). The Nd^{3+} absorption at approximately 580 nm is not observed in this study, likely due to overlapping of Fe^{3+} absorption at the broad band of 500–730 nm (Morris et al., 1985). Our results indicate that Nd^{3+} absorption can be significantly enhanced by processing with the second derivative method (Fig. 7B). The processed spectra generally show a triplet peak (730, 740, and 745 nm) derived from the broad absorption at approximately 740 nm, a doublet peak (794 and 800 nm) derived from the asymmetric absorption at approximately 800 nm, and a single peak derived from the absorption at approximately 865 nm (Fig. 7B).

Table 1. Attribution of Visible Short-Wave Infrared Reflectance Absorptions for Clay Minerals (cf. Bishop et al., 2008, and reference therein)

Wavelength (nm)	Attribution	Related minerals
~960	νOH_{inner} (inner OH stretching), 2nd overtone	Kaolinite, muscovite/illite, smectite/nontronite
~1,396	$\nu OH_{inner\text{-}surface}$ (inner-surface OH stretching), 1st overtone	Kaolinite
1,380–1,440	νOH_{inner}, 1st overtone	Kaolinite, muscovite/illite, smectite/nontronite
~1,910	δH-O-H (molecular water) + νOH	Molecular water-bearing clay minerals (e.g., smectite)
~2,170	$\nu OH_{inner\text{-}surface}$ + δAlAl-OH	Kaolinite
~2,210	νOH_{inner} + δAlAl-OH	Kaolinite, muscovite/illite, smectite
~2,240	νOH_{inner} + δAlFe^{3+}-OH	Fe smectite, Fe kaolinite
~2,270	νOH + δAl-OH	Gibbsite
~2,290	νOH_{inner} + $\delta Fe^{3+}Fe^{3+}$-OH	Fe smectite, nontronite
~2,350/~2,450	Not assigned	Muscovite/illite

Downloaded from http://pubs.geoscienceworld.org/segweb/economicgeology/article-pdf/117/2/495/5505776/4877_tan_et_al.pdf
by Guangzhou Institute of Geochemistry CAS user

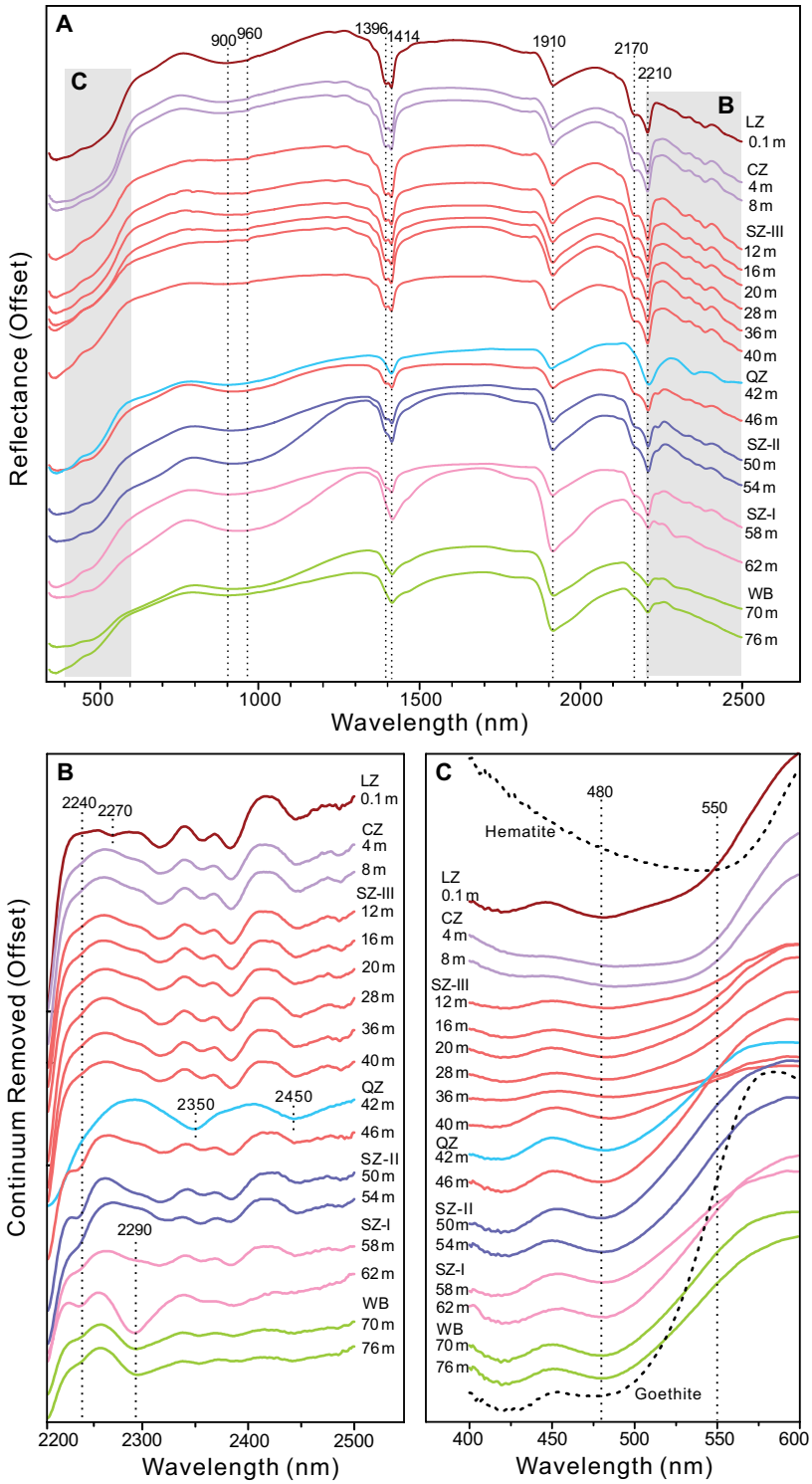

Fig. 6. (A) Original visible short-wave infrared reflectance spectra (350–2,500 nm) of samples from various lithological units of the Renju rare earth element deposit. (B) Continuum-removed reflectance spectra at the band of 220–2,500 nm, derived from the right-shadowed area in (A). (C) Continuum-removed reflectance spectra of Fe-(hydro)oxides at the band of 400–600 nm, derived from the left-shadowed area in (A). Note, curved background of continuum-removed reflectance spectra was transformed into a straight continuum-removed baseline by fitting a quartic or quintic function to the continuum and subtracting it from the spectrum (cf. Cuadros et al., 2016). CZ = completely weathered zone, LZ = lateritic zone, QZ = quartz-rich zone, SZ-I/-II/-III = semiweathered zone I/II/III, WB = weathered bedrock.

Downloaded from http://pubs.geoscienceworld.org/segweb/economicgeology/article-pdf/117/2/495/5505776/4877_tan_et_al.pdf
by Guangzhou Institute of Geochemistry CAS user

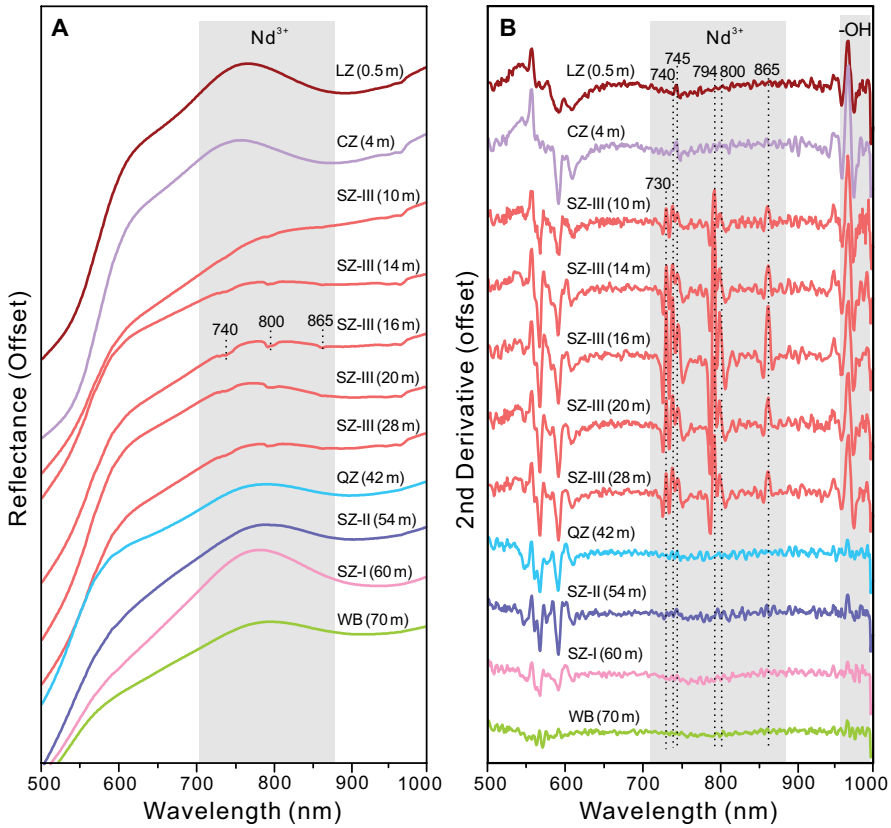

Fig. 7. Original reflectance spectra (A) and corresponding second derivative curves (B) of Nd^{3+}-related absorptions centered at approximately 740, 800, and 865 nm in the visible and near-infrared region range (500–1,000 nm). Note that the position of maxima/minima in the second derivative curves corresponds to an inflection point of the original reflectance spectra, and the maxima highlight a slight change and improve the detection limit for the given Nd^{3+} absorption bands. Concentrations of Nd and total rare earth element (REE) concentrations in different samples: depth at 0.5 m, Nd = 5.8 ppm and total REEs = 623 ppm; depth at 4 m, Nd = 9.7 ppm and total REEs = 319 ppm; depth at 10 m, Nd = 172 ppm and total REEs = 506 ppm; depth at 14 m, Nd = 299 ppm and total REEs = 1001 ppm; depth at 16 m, Nd = 970 ppm and total REEs = 3,348 ppm; depth at 20 m, Nd = 427 ppm and total REEs = 1,665 ppm; depth at 28 m, Nd = 147 ppm and total REEs = 820 ppm; depth at 42 m, Nd = 6.9 ppm and total REEs = 58 ppm; depth at 54 m, Nd = 16 ppm and total REEs = 193 ppm; depth at 60 m, Nd = 113 ppm and total REEs = 569 ppm; depth at 70 m, Nd = 57 ppm and total REEs = 327 ppm. CZ = completely weathered zone, LZ = lateritic zone, QZ = quartz-rich zone, SZ-I/-II/-III = semiweathered zone I/II/III, WB = weathered bedrock.

Discussion

VSWIR indicators for REE concentrations

The VSWIR absorptions of REEs are derived from electron transitions within the 4f configuration (Turner et al., 2014). La^{3+}, Lu^{3+}, Y^{3+}, and Ce^{4+} have no free electrons in their 4f orbitals and thus have no corresponding absorption bands in the VSWIR range. Furthermore, the absorption band of Gd^{3+} is beyond the energy range of VSWIR (Möller and Williams-Jones, 2018; Turner et al., 2018). The absorption bands of Dy^{3+}, Ho^{3+}, Er^{3+}, Tm^{3+}, and Yb^{3+} may overlap the wide absorption bands of Fe in Fe-bearing oxides and clay minerals (Cudahy and Ramanaidou, 1997; Turner et al., 2018) and thus can hardly be observed. The VSWIR absorption bands of Pr^{3+} are observed at approximately 446, 584, and 1,960 nm, those of Sm^{3+} at approximately 404, 970, 1,093, and 1,250 nm, those of Eu^{3+} at approximately 466, 534, 2,079, and 2,183 nm, and those of Tb^{3+} at approximately 2,260 and 2,310 nm (Wang et al., 2017; Möller and Williams-Jones, 2018; Turner et al., 2018). However, the VSWIR absorptions of Pr^{3+}, Sm^{3+}, Eu^{3+}, and Tb^{3+} are not observed in this study (Fig. 7A), likely because of low concentrations of these elements in the regolith (Bao and Zhao, 2008; Sanematsu and Watanabe, 2016; Li et al., 2017).

The maxima of the second derivative curves are obtained from the absorptions of Nd^{3+} at approximately 740, 800, and 870 nm, including M740_2^{nd} from the absorption at approximately 740 nm, M794_2^{nd} and M800_2^{nd} from approximately 800 nm, and M865_2^{nd} from approximately 870 nm (Fig. 7B). The maxima display positive correlations with Nd concentrations measured by ICP-MS (Fig. 8). Given that the absorptions at approximately 740 and 870 nm can overlap the electron absorptions of Fe^{3+} in hematite and goethite (Hunt and Ashley 1979; Cudahy and Ramanaidou, 1997), estimation of Nd concentrations with the two absorptions may cause large uncertainty. In comparison, the spectral parameters M794_2^{nd} (Fig. 9A) and M800_2^{nd} (Fig. 9B) show acceptable sensitivity and accuracy in estimating Nd concentrations of samples from the Renju REE deposit.

Previous investigations have demonstrated that >300 ppm Nd in carbonatites can be detected by VSWIR spectrum (Rowan et al., 1986). Note that the absorption features of

Downloaded from http://pubs.geoscienceworld.org/segweb/economicgeology/article-pdf/117/2/495/5505776/4877_tan_et_al.pdf
by Guangzhou Institute of Geochemistry CAS user

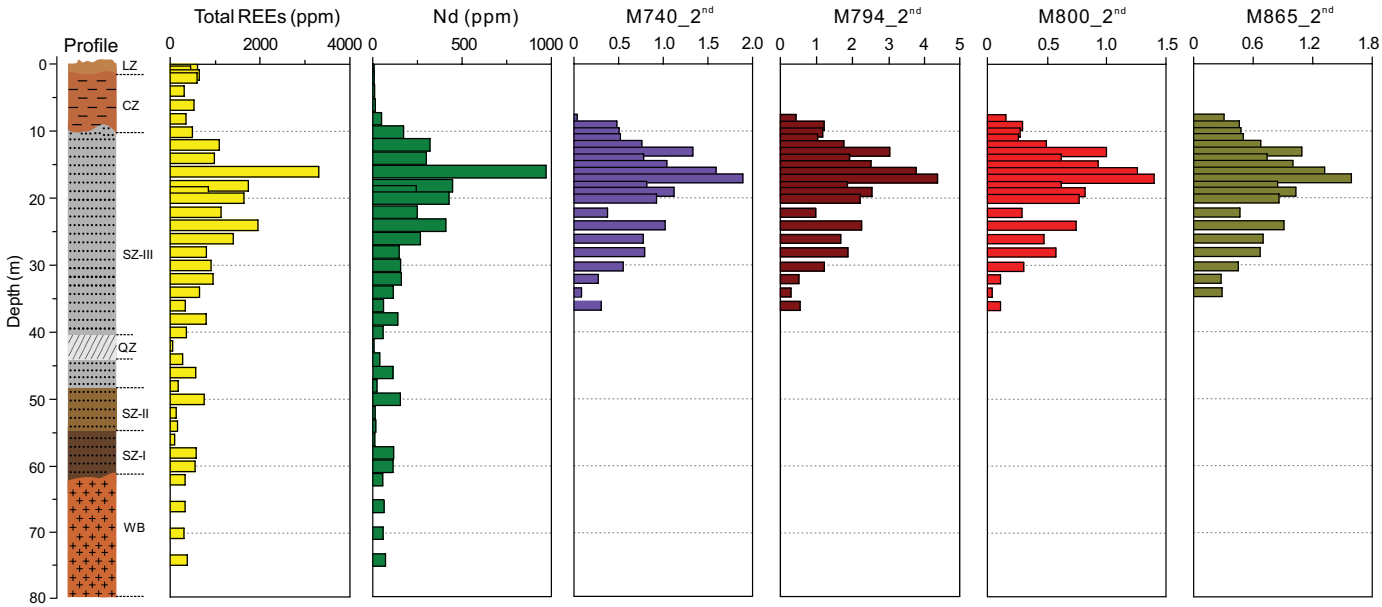

Fig. 8. Total rare earth element (REE) and Nd concentrations of the samples, and values of the visible short-wave infrared reflectance spectral parameters derived from the crystal-field absorption of Nd^{3+} along the profile of the Renju REE deposit. Note: Total REE and Nd concentrations of samples are analyzed by inductively coupled plasma-mass spectrometry. CZ = completely weathered zone, LZ = lateritic zone, QZ = quartz-rich zone, SZ-I/-II/-III = semiweathered zone I/II/III, WB = weathered bedrock.

Fe-rich minerals may overlap the absorption bands of Nd^{3+}, which increases the detection limit of Nd in carbonatites. In contrast, the REE-bearing regolith in Renju typically has relatively low Fe contents, e.g., the kaolinite-rich SZ-III only contains 1–2.5 wt % Fe_2O_3. In addition, the present study suggests that Nd^{3+} absorption signals can be significantly enhanced by processing the original VSWIR spectra with the second derivative method (Fig. 7). As a result, the detection

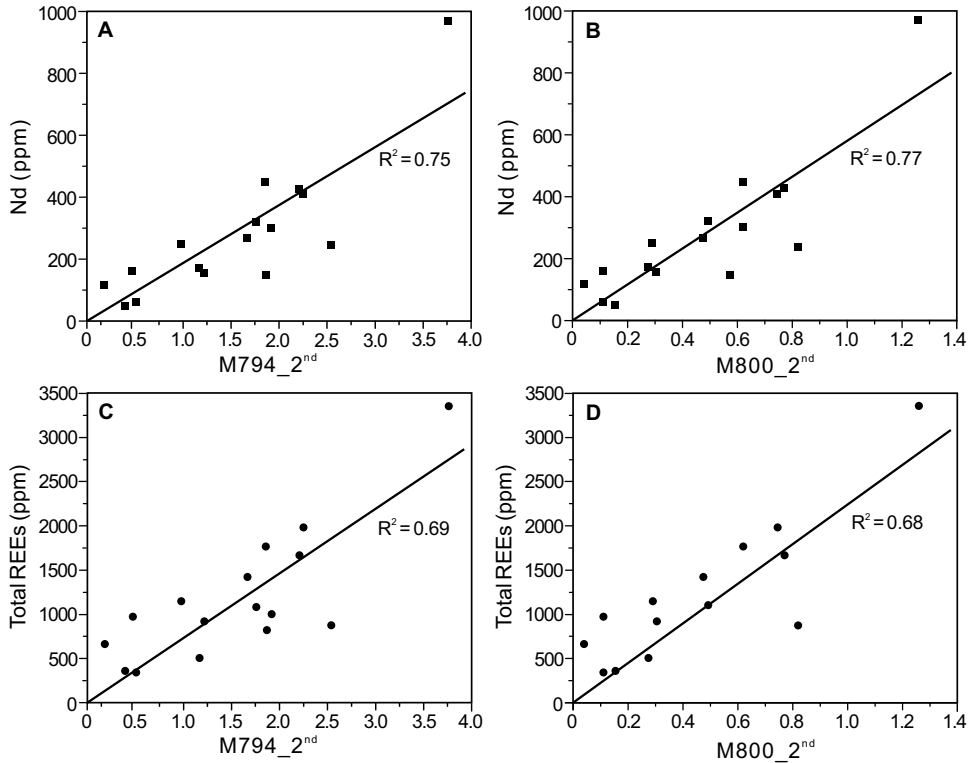

Fig. 9. (A, B) Plots of Nd concentrations in regolith samples versus spectral parameters of M794_2nd and M800_2nd that are derived from crystal-field absorptions of Nd^{3+}. (C, D) Plots of total rare earth element concentrations versus spectral parameters of M794_2nd and M800_2nd. REE = rare earth element.

Downloaded from http://pubs.geoscienceworld.org/segweb/economicgeology/article-pdf/117/2/495/5505776/4877_tan_et_al.pdf
by Guangzhou Institute of Geochemistry CAS user

limit of VSWIR spectroscopy for Nd concentrations is estimated to be approximately 50 ppm according to the spectral response to the variations of Nd concentrations along the profile (Fig. 8).

During the formation of regolith-hosted REE deposits, Nd and other REEs from decomposed REE-bearing minerals are leached and later adsorbed by clay minerals (e.g., kaolinite and halloysite) (Bao and Zhao, 2008). Experimental studies have demonstrated that no obvious fractionation occurs when REEs are adsorbed by kaolinite and halloysite under conditions similar to those of regolith-hosted REE deposits (Yang et al., 2019). As a result, the adsorbed Nd^{3+} generally comprises a fixed proportion (15–25%) of total REE concentrations in the regolith (cf. Li et al., 2017, and references therein). Slight deviation may result from the distinctive geochemical behavior of Ce during mobility and fractionation of other REEs (Nesbitt, 1979). The strong correlations between total REE concentrations and the Nd^{3+}-derived spectral parameters M794_2nd (Fig. 9C) and M800_2nd (Fig. 9D) demonstrate that they can be used to evaluate REE concentrations of a regolith.

VSWIR proxies for weathering intensity

Regolith-hosted REE mineralization commonly occurs in the completely to semiweathered zones in a regolith (Bao and Zhao, 2008; Li et al., 2019). Thus, the weathering intensity is a useful parameter for locating of REE orebodies within a regolith. With progressive weathering, the alkaline (earth) elements in a regolith are gradually leached with the transformation of feldspar and other rock-forming minerals into 2:1-type clay minerals (e.g., illite and smectite), then to 1:1-type clay minerals (e.g., kaolinite and halloysite), and finally to hydroxide minerals (e.g., gibbsite) (Fig. 2). The weathering intensity is essentially related to gradual loss of alkaline (earth) elements and progressive abundance increase and phase transformation of supergene minerals.

The CIA values, reflecting the loss of alkaline (earth) elements during weathering, have been widely used to assess the weathering intensity of a regolith (Nesbitt and Young, 1982). Here, we suggest that the VSWIR parameters that reflect abundances of different supergene minerals can be used to evaluate weathering intensities of a regolith. The band depths of absorptions at 1,396, 1,910, and 1,414 nm in the VSWIR spectra correspond to abundances of kaolinite, smectite, and total clay minerals, respectively (Table 1). The abundances of these clay minerals can be accurately quantified by the maxima on the second derivative curves of the corresponding VSWIR absorptions (i.e., M1396_2nd, M1414_2nd, and M1910_2nd).

The M1396_2nd manifests a positive correlation with abundances of kaolinite as determined by XRD analysis (Fig. 10A). In addition, the highly positive correlation between M1396_2nd and M1414_2nd (Fig. 10B) suggests that the

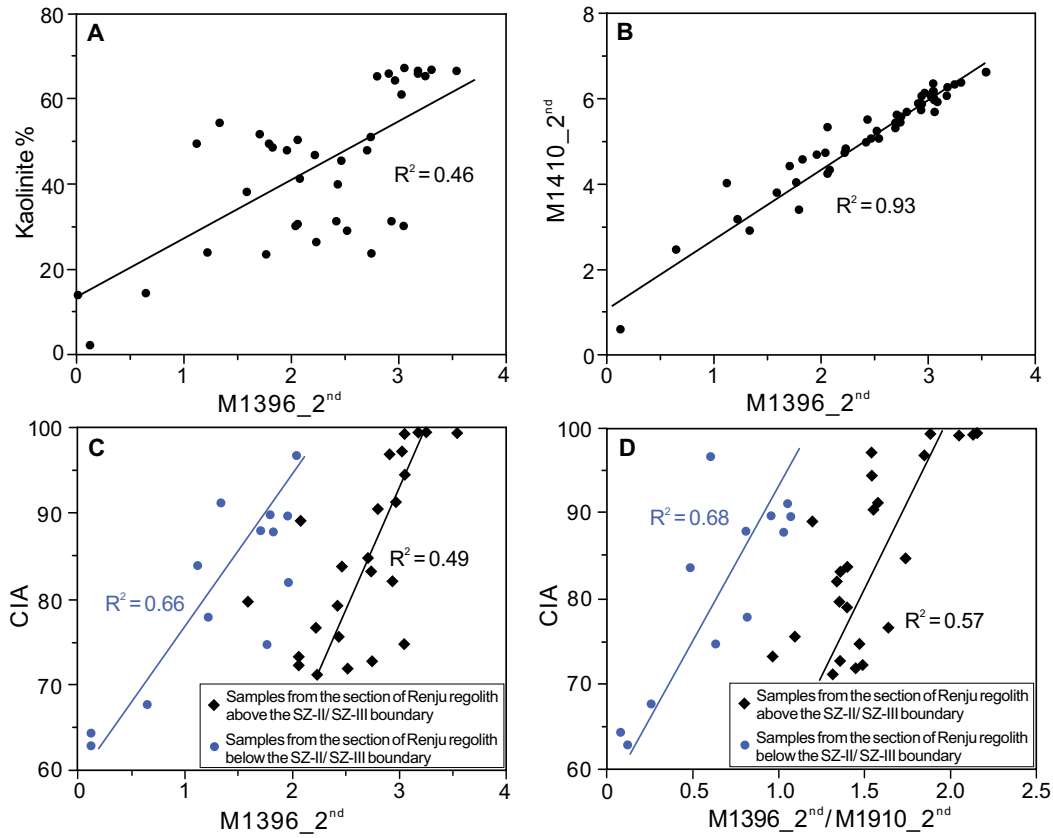

Fig. 10. Correlations between (A) M1396_2nd and abundances of kaolinite determined by X-ray diffraction; (B) M1396_2nd and M1410_2nd; (C) M1396_2nd and CIA; and (D) M1396_2nd/ M1910_2nd and CIA in the Renju profile. Note, M1396_2nd, corresponding to the content of inner-surface OH groups in kaolinite; M1414_2nd, corresponding to the content of inner OH groups in clay minerals. CIA = chemical index of alteration. SZ-I/-II/-III = semiweathered zone I/II/III.

Downloaded from http://pubs.geoscienceworld.org/segweb/economicgeology/article-pdf/117/2/495/5505776/4877_tan_et_al.pdf
by Guangzhou Institute of Geochemistry CAS user

abundance variation of total clay minerals in a regolith is largely determined by kaolinite. Therefore, the M1396_2nd, which is essentially related to the increased abundance of supergene minerals, shows positive correlations with the variation of CIA values in the Renju regolith (Fig. 10C). However, the M1396_2nd is not correlated with CIA values in the lateritic zone (Figs. 3, 11). The CIA values of the topsoil in the Renju regolith commonly approach 100 with the appearance of gibbsite (Fig. 3), whose diagnostic VSWIR absorption occurs at approximately 2,270 nm (Fig. 6B). The CIA values increase with the decomposition of kaolinite into gibbsite at the advanced weathering stage, whereas M1396_2nd gradually decreases with the disappearance of kaolinite.

Comparatively, the M1396_2nd/M1910_2nd ratios reflecting the phase transformation of smectite to kaolinite show a better positive correlation with the CIA values than the M1396_2nd (Fig. 10D), especially at the advanced weathering stage (Fig. 11). As the CIA values of the topsoil can be estimated via petrologic analyses on accessible outcrops, the weathering intensity of a regolith at different depths can thus be quantitatively characterized by referring to the M1396_2nd/M1910_2nd variation. Hence, the M1396_2nd/M1910_2nd ratios can serve as good VSWIR proxies for effective evaluation of the weathering intensities of a regolith.

VSWIR indicators for protolith variation

The REE concentrations, abundances, and compositions of supergene minerals of a regolith are largely determined by primary minerals and weathering intensities of the protolith (Li et al., 2017). However, a regolith may comprise sections that were developed from different protoliths. Thus, recognizing protolith variation in a regolith profile is key to evaluating mineralization and endowment of a regolith-hosted REE deposit. Based on the characteristics of supergene minerals at a different weathering stage, the abundances and composition characteristics of primary minerals in a protolith can be constrained (Dill, 2016).

A regolith that is developed from a homogeneous protolith via progressive weathering commonly displays gradual changes in supergene minerals and weathering intensities and thus tends to display continuous variation trends of related VSWIR parameters. In this study, abrupt changes in the VSWIR parameters of M1396_2nd, M1910_2nd, and M1414_2nd at the SZ-II/SZ-III boundary (Fig. 11) indicate significant variations in abundances of kaolinite, smectite, and total clay minerals, respectively. In addition, a gap at the SZ-II/SZ-III boundary interrupts the continuous trend of the M1396_2nd/M1910_2nd ratios (Fig. 11), which coincides with a fluctuation in the CIA variation trend along the regolith profile (Fig. 3). The M1396_2nd/M1910_2nd ratios also display different increasing slopes (Fig. 11), indicating different weathering rates below and above the SZ-II/SZ-III boundary. Therefore, the spectral features imply that the two sections of regolith below and above the SZ-II/SZ-III boundary likely developed from different protoliths.

The VSWIR parameters reflecting compositional features of Fe-bearing supergene minerals can also serve as

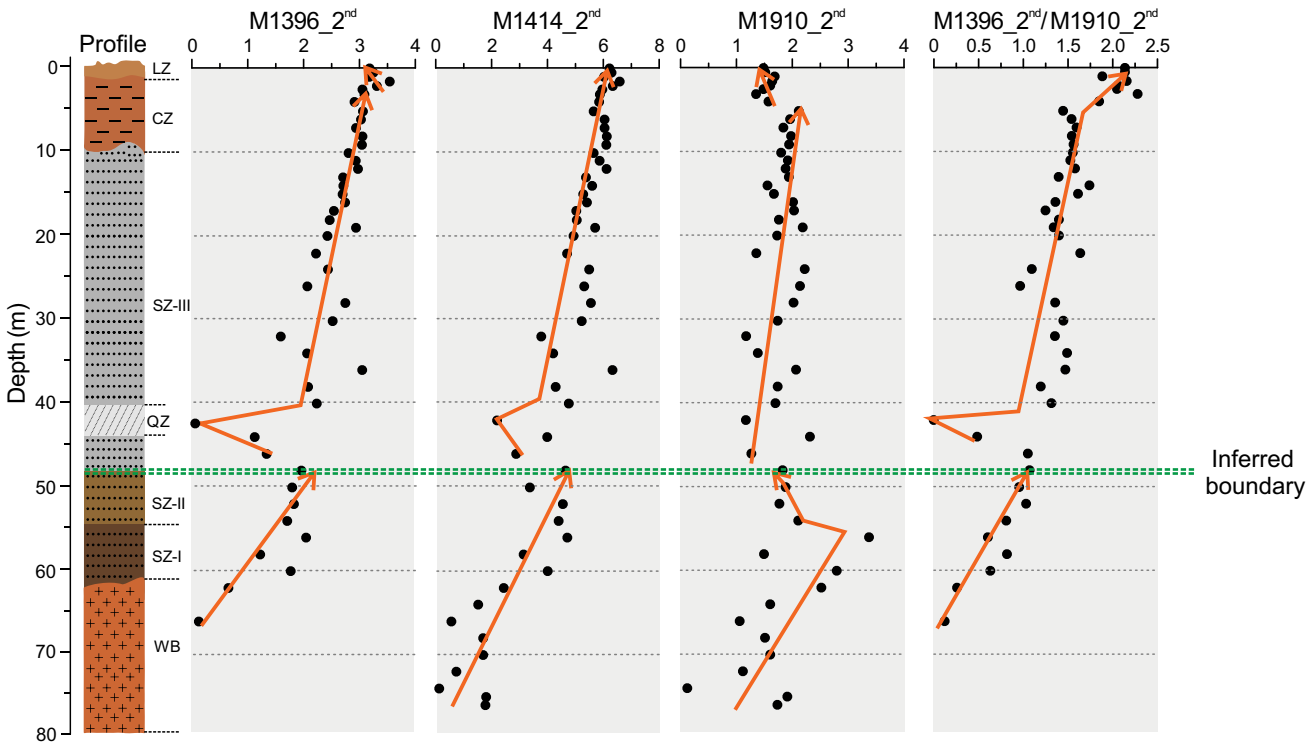

Fig. 11. Spectral parameters that reflect the variation of different types of hydroxyls in clay minerals along the profile of the Renju rare earth element deposit. M1396_2nd, corresponding to the content of inner-surface OH groups in kaolinite; M1414_2nd, corresponding to the content of inner OH groups in clay minerals, including kaolinite, smectite, and illite; M1910_2nd, corresponding to the content of smectite; M1396_2nd/M1910_2nd, corresponding to the content ratio of kaolinite to smectite. CZ = completely weathered zone, LZ = lateritic zone, QZ = quartz-rich zone, SZ-I/-II/-III = semiweathered zone I/II/III, WB = weathered bedrock.

Downloaded from http://pubs.geoscienceworld.org/segweb/economicgeology/article-pdf/117/2/495/5505776/4877_tan_et_al.pdf
by Guangzhou Institute of Geochemistry CAS user

diagnostic indicators to identify protolith variations in a regolith. The VSWIR absorptions of samples below the SZ-II/SZ-III boundary at 2,290 and 2,240 nm demonstrate occurrence of Fe smectite in the slightly weathered bedrock (Fig. 6B). The upward-increasing trend (Fig. 12) and positive correlation between M2240_2nd and P1414 (Fig. 13A) correspond to the increased abundance of Fe-bearing illite and kaolinite with progressive weathering. Formation of Fe-bearing illite and kaolinite is likely due to weathering of chloritized biotite of the quartz dioritic pluton. In contrast, M2240_2nd and P1414 of samples above the SZ-II/SZ-III boundary decrease significantly upward (Fig. 12), indicating that the clay minerals have relatively low Fe contents. In addition, the positive relationship between Fe_2O_3 and BD500 above the SZ-II/SZ-III boundary (Fig. 13B) suggests that Fe has been readily leached from silicate minerals and precipitated as goethite/hematite. The distinctive Fe-bearing supergene minerals below and above the SZ-II/SZ-III boundary reflect significant compositional variations of primary Fe-bearing minerals in their protoliths (Dill, 2016).

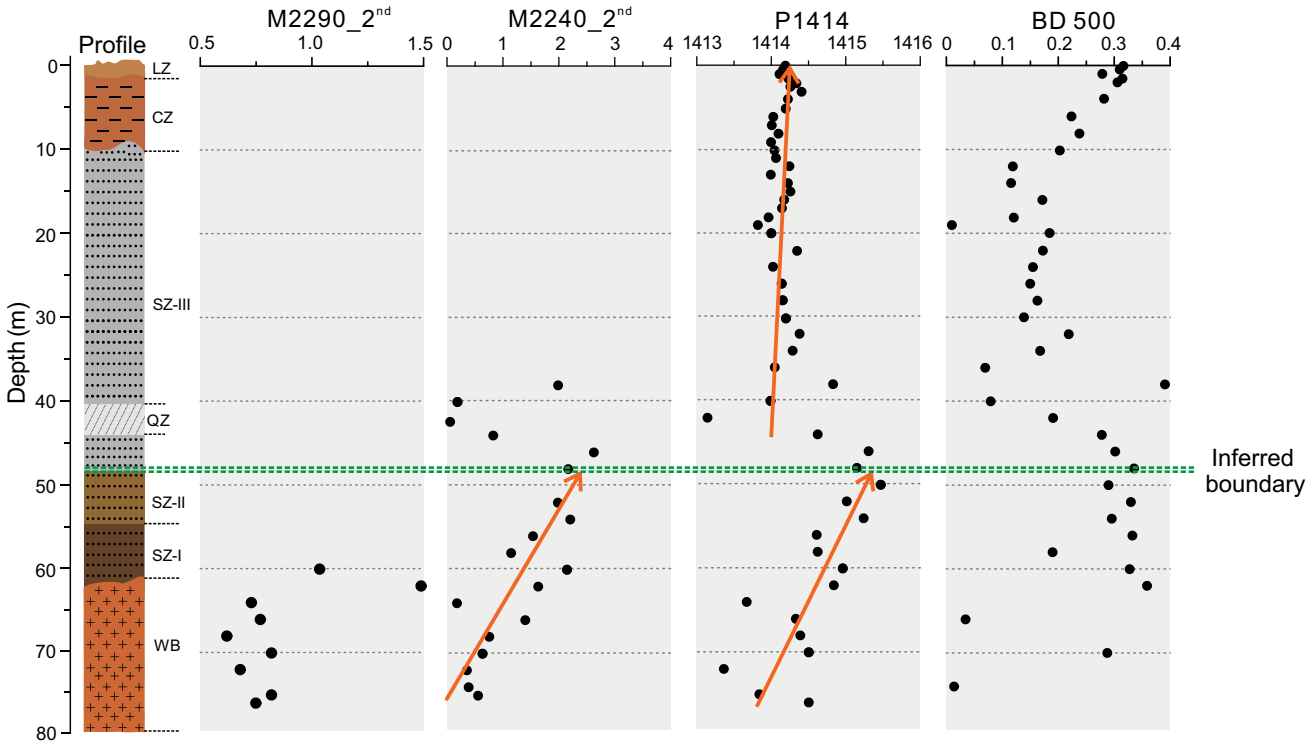

Fig. 12. Spectral parameters that reflect variation trend of visible short-wave infrared reflectance parameters derived from Fe-related absorptions along the profile of the Renju rare earth element deposit. M2290_2nd, corresponding to the content of $Fe^{3+}Fe^{3+}$-OH group in nontronite; M2240_2nd, corresponding to the content of $AlFe^{3+}$-OH groups in nontronite and Fe kaolinite; P1414, position of absorption at approximately 1,414 nm; BD500, band depth of absorption at approximately 500 nm. CZ = completely weathered zone, LZ = lateritic zone, QZ = quartz-rich zone, SZ-I/-II/-III = semiweathered zone I/II/III, WB = weathered bedrock.

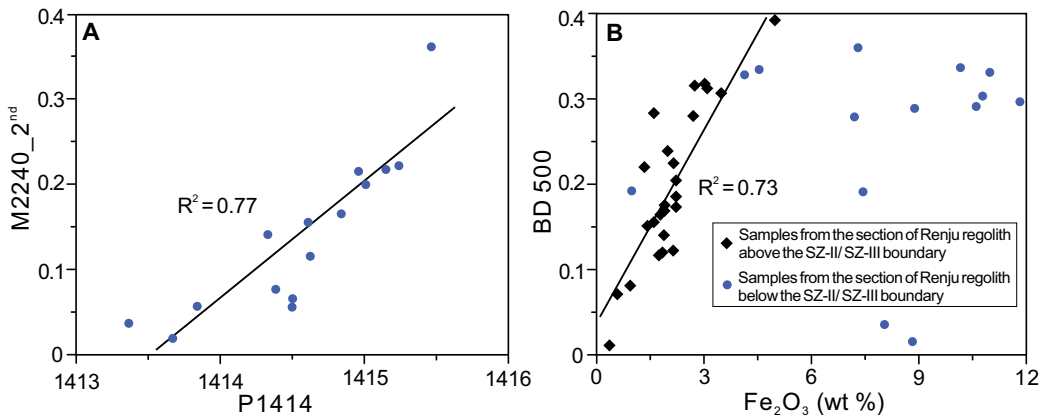

Fig. 13. Plot of P1410 versus M2240_2nd (A) and Fe_2O_3 versus BD500 (B) of samples above and below the SZ-II/SZ-III boundary along the profile of the Renju rare earth element deposit.

Downloaded from http://pubs.geoscienceworld.org/segweb/economicgeology/article-pdf/117/2/495/5505776/4877_tan_et_al.pdf
by Guangzhou Institute of Geochemistry CAS user

The Renju regolith is underlain by a quartz dioritic pluton (Fig. 1). The regolith below the SZ-II/SZ-III boundary was probably developed from the dioritic pluton. However, the dioritic pluton could be overlain by other igneous rocks (e.g., rhyolite tuff) in the Renju region (Fig. 1). In view of the Fe_2O_3 content along the profile (Fig. 3), the regolith above the SZ-II/SZ-III boundary was likely developed from biotite granite and/or rhyolite tuff (Fig. 1). Weathering of the overlying igneous rocks possibly formed the regolith comprising the SZ-III, the completely weathered zone, and the lateritic zone, which displays continuous variation trends of VSWIR parameters (Fig. 11). Development of deposit-scale faults (Fig. 1) possibly resulted in the complex vertical distribution of igneous rocks in this region.

Conclusions

This study demonstrates that spectral parameters can serve as diagnostic indicators for prospecting regolith-hosted deposits. The M794_2nd and M800_2nd derived from the crystal-field absorptions of Nd^{3+} at approximately 800 nm can serve as reliable VSWIR proxies for the assessment of REE grades of orebodies in regolith that hosts REE deposits.

The M1396_2nd/M1910_2nd ratios can effectively reflect the evolution of clay minerals with progressive weathering and thus provide information about weathering intensities and about REE-fertile sections in a regolith profile.

The variation trends of spectral parameters of M1396_2nd/M1910_2nd, M2290_2nd, M2240_2nd, P1414, and BD500, and other spectral parameters that indicate the abundances and compositions of supergene minerals and weathering intensity can reveal variation of the protolith forming different sections of a regolith.

Acknowledgments

This work was financially supported by the National Key R&D Program of China (grant 2017YFC0602306), National Natural Science Foundation of China (grant 91962216), the Key Research Program of the Institute of Geology and Geophysics, Chinese Academy of Sciences (grant IGGCAS-201901), Science Research Program of Guangzhou, China (grant 201804020037), Department of Science and Technology of Guangdong Province (grant 2017GC010578), and the Science and Technology Planning Project of Guangdong Province, China (grant 2017B030314175/2020B1212060055). We thank Benard Hubbard and Zhaoshan Chang for constructive comments and the editors for handling our manuscript. This is contribution IS-3038 from Guangzhou Institute of Geochemistry, Chinese Academy of Sciences.

REFERENCES

Bao, Z., and Zhao, Z., 2008, Geochemistry of mineralization with exchangeable REY in the weathering crusts of granitic rocks in South China: Ore Geology Reviews, v. 33, p. 519–535.

Bishop, J.L., Lane, M.D., Dyar, M.D., and Brown, A.J., 2008, Reflectance and emission spectroscopy study of four groups of phyllosilicates: Smectites, kaolinite-serpentines, chlorites and micas: Clay Minerals, v. 43, p. 35–54.

Chang, Z., and Yang, Z., 2012, Evaluation of inter-instrument variations among short wavelength infrared (SWIR) devices: Economic Geology, v. 107, p. 1479–1488.

Clark, R.N., King, T.V.V., Klejwa, M., and Swayze, G.A., 1990, High spectral resolution reflectance spectroscopy of minerals: Journal of Geophysical Research, v. 95, p. 12,653–12,690.

Cuadros, J., Michalski, J.R., Dekov, V., and Bishop, J.L., 2016, Octahedral chemistry of 2:1 clay minerals and hydroxyl band position in the near-infrared: Application to Mars: American Mineralogist, v. 101, p. 554–563.

Cudahy, T.J., 2016, Mineral mapping for exploration: An Australian journey of evolving spectral sensing technologies and industry collaboration: Geosciences v. 52, p. 1–48.

Cudahy, T.J., and Ramanaidou, E.R., 1997, Measurement of the hematite:goethite ratio using field visible and near-infrared reflectance spectrometry in channel iron deposits, Western Australia: Journal of the Geological Society of Australia, v. 44, p. 411–420.

Delineau, T., Allard, T., Muller, J.C., Barres, O., Yvon, J., and Cases, J.M., 1994, FTIR reflectance vs. EPR studies of structural iron in kaolinites: Clay and Clay Minerals, v. 42, p. 308–320.

Dill, H.G., 2016, Kaolin: Soil, rock and ore from the mineral to the magmatic, sedimentary and metamorphic environments: Earth Science Reviews, v. 161, p. 16–129.

Herrmann, W., Blake, M., Doyle, M., Huston, D., Kamprad, J., Merry, N., and Pontual, S., 2001, Short wavelength infrared (SWIR) spectral analysis of hydrothermal alteration zones associated with base metal sulfide deposits at Rosebery and Western Tharsis, Tasmania, and Highway-Reward, Queensland: Economic Geology, v. 96, p. 939–955.

Hunt, G.R., 1977, Spectral signatures of particulate minerals in the visible and around infrared: Geophysics, v. 42, p. 501–513.

Hunt, G.R., and Ashley, R.P., 1979, Spectra of altered rocks in the visible and near infrared: Economic Geology, v. 74, p. 1613–1629.

Jansen, N.H., Cooke, D.R., Harris, A.C., and McKnight, S.W., 2017, Near-infrared effectiveness on degraded core in tropical climates: Economic Geology, v. 112, p. 1011–1019.

Jones, S., Herrmann, W., and Gemmell, J.B., 2005, Short wavelength infrared spectral characteristics of the HW horizon: Implications for exploration in the Myra Falls volcanic-hosted massive sulfide camp, Vancouver Island, British Columbia, Canada: Economic Geology, v. 100, p. 273–294.

Li, M.Y.H., Zhou, M.F., and Williams-Jones, A.E., 2019, The genesis of regolith-hosted heavy rare earth element deposits: Insights from the world-class Zudong deposit in Jiangxi Province, South China: Economic Geology, v. 114, p. 541–568.

Li, Y.H.M., Zhao, W.W., and Zhou, M.F., 2017, Nature of parent rocks, mineralization styles and ore genesis of regolith-hosted REE deposits in South China: An integrated genetic model: Journal of Asian Earth Sciences, v. 148, p. 65–95.

Liu, J., He, H., Michalski, J., Cuadros, J., Yao, Y., Tan, W., Qin, X., Li, S., and Wei, G., 2021, Reflectance spectral study of secondary mineralogical evolution and weathering intensity of a thick basaltic weathering sequence in Hainan Island, South China: Applied Clay Science v. 201, article 105923.

Mathian, M., Heber, B., Baron, F., Petit, S., Lescuyer, J.L., Furic, R., and Beaufort, D., 2018, Identifying the phyllosilicate minerals of hypogene ore deposits in lateritic saprolites using the near-IR spectroscopy second derivative methodology: Journal of Geochemical Exploration, v. 186, p. 298–314.

Meng, L., Zhang, Z., Wu, Y., Liu, J., Shao, F., Hua, J., and Chen, R., 2016, The geochemistry features and petrogenesis of Dabu Caledonian granite in southern Jiangxi province: Uranium Geology, v. 32, p. 13–22 (in Chinese with English abs.).

Möller, V., and Williams-Jones, A.E., 2018, A hyperspectral study (V-NIR-SWIR) of the Nechalacho REE-Nb-Zr deposit, Canada: Journal of Geochemical Exploration, v. 188, p. 194–215.

Morris, R.V., Lauer Jr., H.V., Lawson, C.A., Gibson Jr., E.K., Nace, G.A., and Stewart, C., 1985, Spectral and other physicochemical properties of submicron powders of hematite $\gamma(\alpha\text{-}Fe_2O_3)$, maghemite $(\gamma\text{-}Fe_2O_3)$, magnetite (Fe_3O_4), goethite $(\alpha\text{-FeOOH})$, and lepidocrocite $(\gamma\text{-FeOOH})$: Journal of Geophysical Research, v. 90, p. 3126–3144.

Neave, D.A., Black, M., Riley, T.R., Gibson, S.A., Ferrier, G., Wall, F., and Broom-Fendley, S., 2016, On the feasibility of imaging carbonatite-hosted rare earth element deposits using remote sensing: Economic Geology, v. 111, p. 641–665.

Nesbitt, H.W., 1979, Mobility and fractionation of rare earth elements during weathering of a granodiorite: Nature, v. 279, p. 206–210.

Nesbitt, H.W., and Young, G.M., 1982, Early Proterozoic climates and plate motions inferred from major element chemistry of lutites: Nature, v. 299, p. 715–717.

Ramanaidou, E., Wells, M., Lau, I., and Laukamp, C., 2015, Characterization of iron ore by visible and infrared reflectance and, Raman spectroscopies *in* Lu, L., ed., Iron ore: Mineralogy, processing and environmental sustainability: Amsterdam, Elsevier, p. 191–228.

Downloaded from http://pubs.geoscienceworld.org/segweb/economicgeology/article-pdf/117/2/495/5505776/4877_tan_et_al.pdf
by Guangzhou Institute of Geochemistry CAS user

Ramsey, M.H., Potts, P.J., Webb, P.C., Watkins, P., Watson, J.S., and Coles, B.J., 1995, An objective assessment of analytical method precision: Comparison of ICP-AES and XRF for the analysis of silicate rocks: Chemical Geology, v. 124, p. 1–19.

Regional Geological Survey Team of Jiangxi Geological Bureau, 1976, Report of 1:200,000 regional geological survey of the Xunwu region: Anyuan (in Chinese).

Rowan, L.C., Kingston, M.J., and Crowley, J.K., 1986, Spectral reflectance of carbonatites and related alkalic igneous rocks; selected samples from four North American localities: Economic Geology, v. 81, p. 857–871.

Sanematsu, K., and Watanabe, Y., 2016, Characteristics and genesis of ion adsorption-type rare earth element deposits: Reviews in Economic Geology, v. 18, p. 55–79.

Schwertmann, U., and Cornell, R.M., 2008, The iron oxides, *in* Schwertmann, U., and Cornell, R.M., eds., Iron oxides in the laboratory: Preparation and characterization: Hoboken, New Jersey, Wiley, p. 5–13.

Tamer, M., 2013, Quantitative phase analysis based on Rietveld structure refinement for carbonate rocks: Journal of Modern Physics, v. 4, p. 1149–1157.

Turner, D.J., Rivard, B., and Groat, L.A., 2014, Visible and short-wave infrared reflectance spectroscopy of REE fluorocarbonates: American Mineralogist, v. 99, p. 1335–1346.

——2016, Visible and short-wave infrared reflectance spectroscopy of REE phosphate minerals: American Mineralogist, v. 101, p. 2264–2278.

——2018, Visible and short-wave infrared reflectance spectroscopy of selected REE-bearing silicate minerals: American Mineralogist, v. 103, p. 927–943.

Wang, C., Zhang, T., and Pan, X., 2017, Potential of visible and near-infrared reflectance spectroscopy for the determination of rare earth elements in soil: Geoderma, v. 306, p. 120–126.

Xie, Y., Hou, Z., Goldfarb, R.J., Guo, X., and Wang, L., 2016, Rare earth element deposits in China: Reviews in Economic Geology, v. 18, p. 115–136.

Xu, C., Kynicky, J., Smith, M.P., Kopriva, A., Brtnicky, M., Urubek, T., Yang, Y., Zhao, Z., He, C., and Song, W., 2017, Origin of heavy rare earth mineralization in South China: Nature Communications, v. 8, p. 1–7.

Yang, D.H., and Xiao, G.M., 2011, Regional metallogenic regularities of the ion adsorption type of rare-earth deposits in Guangdong province: Geology and Resources, v. 20, p. 462–468 (in Chinese with English abs.).

Yang, M., Liang, X., Ma, L., Huang, J., He, H., and Zhu, J., 2019, Adsorption of REEs on kaolinite and halloysite: A link to the REE distribution on clays in the weathering crust of granite: Chemical Geology, v. 525, p. 210–217.

Wei Tan is an assistant researcher at the Key Laboratory of Mineralogy and Metallogeny, Guangzhou Institute of Geochemistry, Chinese Academy of Sciences. He received his Ph.D. degree in mineralogy, petrology, and geochemistry from the University of Chinese Academy of Sciences (Beijing) in 2016 and was a visiting research fellow at the School of Earth and Planetary Sciences, Curtin University (2018–2019). His research interests focus on microstructural, geochemical, and spectral characteristics of economic minerals, genetic links between diagnostic minerals and related metallogenic systems, and application of indicator minerals in exploration.

Downloaded from http://pubs.geoscienceworld.org/segweb/economicgeology/article-pdf/117/2/495/5505776/4877_tan_et_al.pdf
by Guangzhou Institute of Geochemistry CAS user